

Fractional quantum Hall effect and Wigner crystallization in suspended Corbino graphene disk

Manohar Kumar, Antti Laitinen, and Pertti J. Hakonen

*Low Temperature Laboratory, Department of
Applied Physics, Aalto University, Espoo, Finland*

Abstract

Competition between liquid and solid states in two-dimensional electron system is an intriguing problem in condensed matter physics. At high magnetic fields, the kinetic energy of electrons is suppressed, which favors Wigner crystallization of electrons to a lattice. However, electrons commonly favor an incompressible liquid state, the fractional quantum Hall (FQH) liquid, instead of the Wigner crystal solid phase. We have investigated competing Wigner crystal and FQH liquid phases in atomically thin suspended graphene devices in Corbino geometry, where no topological edge states contribute to the current driven through the sample. Low-temperature magnetoconductance and transconductance measurements along with IV characteristics all indicate strong charge-density-dependent modulation of electron transport. Our results indicate FQH phases in a re-entrant fashion around crystalline order at filling factors $0.12 - 0.20$. Building on the unique sample structure, our experiments pave the way for enhanced understanding of the ordered phases of interacting electrons in two dimensions.

The fractional quantum Hall (FQH) state is a many body phenomenon where elementary excitations are composite fermions with fractional electronic charge leading to quantization of the Hall conductance at fractional filling factor $\nu = n/(B/\phi_0)$ at carrier density n and magnetic field B (flux quantum $\phi_0 = h/e$) [1]. The manifestation of these exotic states requires a large Coulomb interaction energy compared with the disorder potential, putting strict requirements for the quality of the two-dimensional electron gas (2-DEG), the strength of the magnetic field, and for excitation by environmental noise or temperature. Owing to reduced screening in atomically thin graphene, the electrons in graphene interact with higher Coulomb interaction energy than electrons in conventional semiconductor heterostructures, providing an extraordinary setting for FQH effect. Such states were first discerned in rectangular, two-terminal, high-mobility suspended graphene devices [2, 3], where a quantized conductance corresponding to the $\nu = 1/3$ FQH state was observed and, subsequently, characterized in terms of the energy gap [4]. However, due to intermixing of ρ_{xy} and ρ_{xx} [5], it has turned out to be difficult to observe FQH states in rectangular two-lead suspended graphene [6] and most of the quantum Hall studies have been performed using supported samples in Hall bar geometry.

Multi-terminal transport measurements on G/h-BN performed in magnetic fields up to 35 T have revealed several FQH states whose filling factors are mostly integer multiples of $1/3$, (*i.e.* $1/3 \dots 13/3$) [7, 8]; many of these states have recently been identified also in local compressibility measurements in suspended graphene using scanning SET techniques [9, 10] and two-lead transconductance experiments [11]. In spite of the experimental challenges, higher Coulomb interaction energy in suspended graphene [12] makes suspended sample a very attractive platform to probe the interaction-based physics in conjunction with mechanical motion [13] as well as to investigate the competition between the lowest order FQH states and Wigner crystal type of ordering [14, 15].

We have fabricated suspended graphene Corbino disks for probing correlated many-body physics in graphene at high fields. The Corbino geometry has a distinct advantage over the regular Hall bar geometry, as it directly probes the bulk two-dimensional electron gas (2-DEG) without complications due to edge state transport. In this geometry, the quantum Hall edge states counter propagate at the perimeters of Corbino disk and no edge channel is formed between the two electrodes. The very first proposal of Corbino geometry to study quantum Hall states was put forth by Laughlin [16] who considered the role of azimuthal

currents induced by varying flux through the loop. Since then, a number of experimental studies of magneto-transport in Corbino geometry have been performed using semiconductor heterostructures [17–20] and, recently, also using graphene in which the research focus has been on temperature dependent magneto-conductance behavior in the quantum Hall regime [21, 22]. These previous measurements on graphene Corbino disks have failed to show any fractional states, perhaps due to strong charge inhomogeneity induced by the substrate.

Contrary to earlier approach, our experiments at mK temperatures were conducted on current-annealed suspended graphene Corbino disks, where conductance is fully governed by either activation or tunneling across FQH states localized on disorder potential. In our magneto- and transconductance measurements, we resolved a distinctive set of incompressible liquid states with fractional filling factors of $\{2/7, 1/3, 2/5, 3/7, 4/9, 4/7, 3/5, 2/3, 4/5, 9/7, 4/3\}$, on top of which we could resolve evidence of solid phase order. Our $I(V)$ measurements indicate Wigner crystallization of electrons at low density around $\nu = 0.12 - 0.20$, bordered in a re-entrant fashion by the FQH states. The IV characteristics in the FQH regime also point towards significance of co-tunneling processes across multiple localized states at high bias.

I. SAMPLES AND BASIC EXPERIMENTAL RESULTS

Our sample structure is illustrated in Fig. 1a. The suspended graphene disk is only supported by the inner and outer Au/Cr leads. The basic characteristics of our samples after current cleaning are displayed Table I. The conductivity was calculated from the measured conductance G using $\sigma = \frac{G}{2\pi} \ln(r_o/r_i)$, (see, *e.g.* Ref. [19]), where r_o and r_i are the radii of outer and inner contacts, respectively. The field-effect mobility was determined using equation $\mu_f = \frac{\tilde{\sigma} - \tilde{\sigma}_0}{ne}$ where $\tilde{\sigma}$ is the conductivity after subtracting out the contact resistance and $\tilde{\sigma}_0$ denotes its value at the Dirac point ($V_g = V_g^d \simeq -1$ V) [23]. The residual charge density n_0 was identified by looking for a cross-over between constant and power law behavior in $\log G$ *vs.* $\log n$ traces. Details concerning determination of basic parameters are given in the supplemental information [23] which also describes the major steps in sample fabrication.

In zero magnetic field, the conductance of graphene in Corbino geometry at V_g^d equals to $G = \frac{8e^2}{h} \log(\frac{r_o}{r_i})^{-1}$ according to conformal mapping theory [24]. After subtraction of

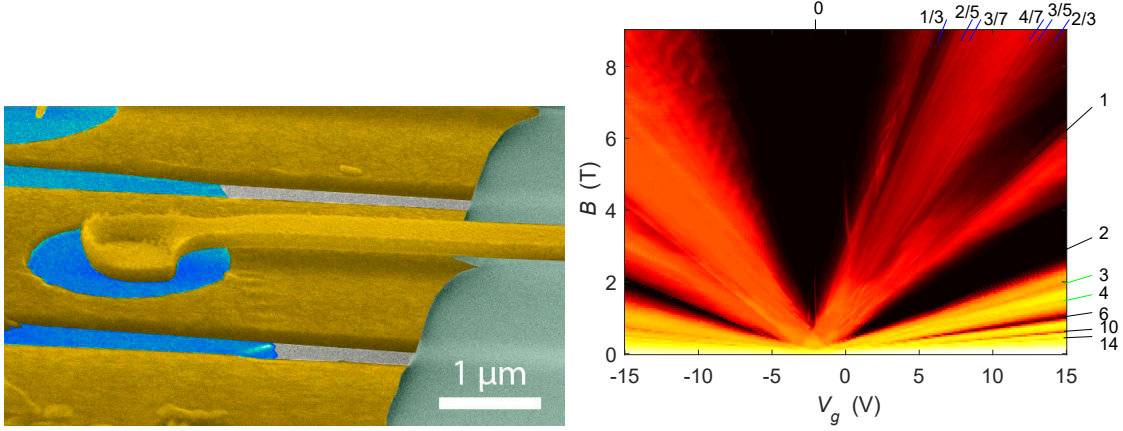


FIG. 1. (a) Scanning electron micrograph of a 2- μm -diameter graphene Corbino sample (XD) with 700 nm diameter circular middle contact; blue denotes the suspended graphene while gold appears as grayish yellow. The white scale bar corresponds to 1 μm . Note that the sample is supported only by the gold/chromium contacts at the edges, see Fig. 1g of the supplemental information. (b) The logarithmic magneto-conductance of sample EV (see Table I) measured using AC peak-to-peak excitation current $I_{p-p} = 0.1$ nA at 20 mK, displayed as a Landau fan diagram on the B vs. charge density n plane. The blue lines at $\nu = nh/eB$ identify FQH states $\nu = \{1/3, 2/5, 3/7, 4/7, 3/5, 2/3\}$ (further FQH states are found in transconductance data) and broken symmetry states $\nu = \{0, 1, 3, 4\}$. Here charge density ranges over $n = -1.1 \times 10^{11} \dots +1.5 \times 10^{11} \text{ cm}^{-2}$.

the contact resistance, our measured conductivity is in line with the above theoretical value. Furthermore, the measured gate voltage dependence of $G(V_g)$ in the unipolar regime is found to agree with theoretical formulas [23].

In our samples, we observed broken symmetry states ($\nu = 0, 3, 4$) down to 0.6 Tesla, indicating our samples are of very high quality. The basic Landau fan diagram measured on sample EV (see Table I) is illustrated in Fig. 1b. In addition to several integer Landau levels, the fractional states $1/3, 2/5, 3/7, 4/7, 3/5$, and $2/3$ are visible on the electron side but not clearly on the hole side. Consequently, in the text below we concentrate on the FQH states on the electron side.

II. LOCALIZED STATES IN THE FQH REGIME

Impurities and uncontrolled charge doping create a disorder potential in suspended graphene. The disorder potential and variation in charge density give rise to formation of localized states as illustrated in Fig. 2. These states are formed to regions where the charge density does not lead to complete filling of a fractional quantum Hall state [25, 26]. An incompressible FQH liquid surrounds the localized states, inside which free rearrangement of charge leads to a constant electrochemical potential. At the border of the incompressible FQH zone around a local compressible region there will be a current carrying edge state that closes to itself. Such edge states can carry current across the sample only via coupling, either by quantum tunneling or thermal activation, to adjacent localized states. Charge in elementary units can be added into the localized states one by one, and thus such states behave quite like quantum dots in semiconducting devices. In the case of weak screening, these localized states interact electrostatically with many nearby localized states. Charge fluctuations among the interacting quantum dots lead to broadening of the energy levels, which enhances overlap of adjacent quantum dot wave functions and thereby tunneling conductance through the localized states by quantum tunneling at low T .

Theoretical models in the case of a long-range random disorder potential predict thermally activated conductivity, $\sigma = A \exp(-U_s/2k_B T)$, where the activation energy U_s is proportional to the gap Δ_l in FQH states and the prefactor $A \simeq (e^*)^2/h$ is governed by effective charge e^* of charge carriers [27, 28]; in thermal activation, the effective charge is related to the filling factor $e^* = \nu e$ [27, 28], whereas in quantum tunneling regime it may be either νe or e [29]. In a similar approximative approach, the conductivity in the quantum tunneling regime can be expressed as $\sigma = A \exp(-U_s/2k_B T_{cr})$, where T_{cr} denotes the cross-over temperature between thermal activation and quantum tunneling. The cross-over temperature is difficult to determine theoretically but it can be estimated from the saturation temperature of $\sigma(T)$ scans, which in our experiments varies in the range $T = 1 - 0.5$ K.

Charging effects of localized states can be employed for detection of the fragile FQH states that are formed locally in the bulk [25]. Charging effects lead to sets of modulation patterns on transconductance $g_m(B, n) = dI/dV_g$ maps which facilitates identification of localized states by pattern recognition and classification by dominant filling factors [11]. As seen in

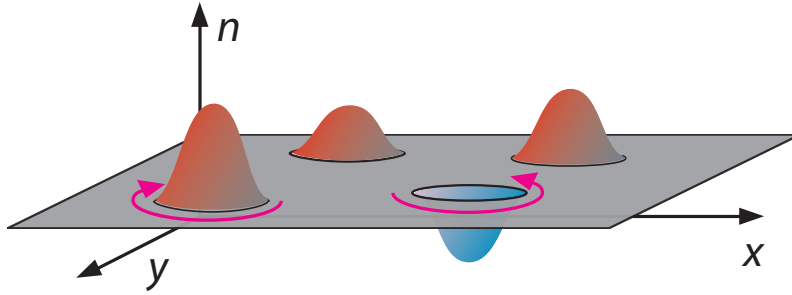


FIG. 2. Schematic picture of localized states with variation in charge density marked in red (enhanced density) and blue (reduced density). The localized states are embedded within the incompressible FQH liquid with constant electron density (gray plane). Landau levels (LLs) are bending upwards when approaching the blue regions while they bend down around the red bumps. Consequently, skipping orbits of edge state electrons reside outside and inside the borders of the low and high density regions, respectively. Magenta arrows mark the directions of the currents of these localized edge states. Electric transport at low temperatures takes place via quantum tunneling between the localized states through a barrier due to the energy gap Δ_l of the incompressible FQH region. In case of considerable variation of charge (*i.e.* the red dips/hillocks reaching the next FQH charge density plane), there will be additional localized fractional states within such regions. Since these states are localized within a bounded region with an edge state, their effect on charge transport can be neglected.

Fig. 3a, both FQH and QH states, localized on disorder potential landscape, are observed as additional sets of parallel lines in our $g_m(B, n)$ scans. The slope of the fringes varies in non-monotonic fashion, which is indicative of features coming from spatially-modulated charge density due to disorder potential.

The fringe pattern of Fig. 3a has been treated using a correlation analysis described in the supplement [23]. The raw cross-correlation value *i.e.* $h(\nu) = \sum_{\nu=\text{const.}} g_{m_i} * g_{m_j} (1 - \delta_{i,j}) / S$ amounts to the total sum of product of two g_m values evaluated along all pixel lines of points (n_i, B_i) for which the slope $\Delta n_i / \Delta B_i$ equals to the filling factor ν ; the Kronecker delta cuts out the autocorrelation part of the correlation function and the number of summed products

S is used as the scaling factor. This process was repeated for all values of $\nu = 0.2 - 1.1$ in order to determine the distribution of scaled correlation function $c(\nu) = h(\nu)/h(\nu)_{max}$. These distributions were determined using g_m data scanned over eight vertical areas on $n-B$ plane (Fig. 3a), and the resulting $c(\nu)$ distributions are displayed in Fig. 3b; in order to enhance contrast of $\nu = 2/3$ and $\nu = 3/7$ fringes, two inclined regions were also analyzed (see Fig. 3a). Clear maxima at the strongest fractional states are visible in Fig. 3b. We are able to identify fractional fillings $\{2/7, 1/3, 2/5, 3/7, 4/9, 4/7, 3/5, 2/3\}$ for the bulk FQH states, in agreement with our magneto-conductance measurements. A summary of the FQH states identified by G and g_m measurements in our three Corbino samples is shown in Table I. The comparison of different results in Table I clearly demonstrates that $g_m(n, B)$ measurement is superior over simple magneto-conductance measurement in probing fragile fractional states in the bulk, and it is instrumental in studies of disordered samples.

Sample	r_i/r_o in μm	n_o $1/\text{cm}^2$	μ_f cm^2/Vs	σ_0 S	Measurement	FQH states
XD	0.35/1.0	2×10^{10}	4.0×10^4	1.6×10^{-5}	g_m and G	$\{\frac{1}{3}, [\frac{2}{5}], [\frac{4}{7}], \frac{2}{3}, [\frac{4}{5}], [\frac{4}{3}]\}$
EV	0.40/1.6	6×10^9	2.0×10^5	1.4×10^{-4}	g_m and G	$\{[\frac{2}{7}], \frac{1}{3}, \frac{2}{5}, \frac{3}{7}, [\frac{4}{9}], \frac{4}{7}, \frac{3}{5}, \frac{2}{3}\}$
EV*	0.40/1.6	6×10^9	1.4×10^5	1.1×10^{-4}	G and $\delta G/\delta n$	$\{\frac{1}{3}, \frac{2}{5}, \frac{3}{7}, \frac{4}{7}, \frac{3}{5}, \frac{2}{3}, \frac{4}{5}, \frac{9}{7}\}$

TABLE I. Characteristics of our suspended Corbino graphene samples (by columns): inner and outer radii r_i and r_o , respectively, n_0 is the residual charge density, field effect mobility μ_f is measured at $n \sim 8 \times 10^{10} 1/\text{cm}^2$, and σ_0 denotes the minimum conductivity; the contact resistance R_C was subtracted off from the conductivity only when calculating μ_f . The FQH states probed by g_m are indicated by square brackets $[p/q]$, otherwise the identification is based on magneto-conductance G . EV* corresponds to a measurement done on sample EV in its second cool down, in which a change in FQH detection is observed along with decreased mobility.

The data in Fig. 3a display also clear fringes with slopes $\nu = 1$ and 2 overlaid in the middle of the picture on the bulk fringes. This co-existence of fringes representing different filling factors ν requires the local charge density $n_{loc} > eB/h$. Furthermore, these slopes are by far off from the possible slopes facilitated by the width of the residual charge distribution based on $\log G(V_g)$ analysis. Hence, we conclude that $\nu = 1$ and 2 fringes are

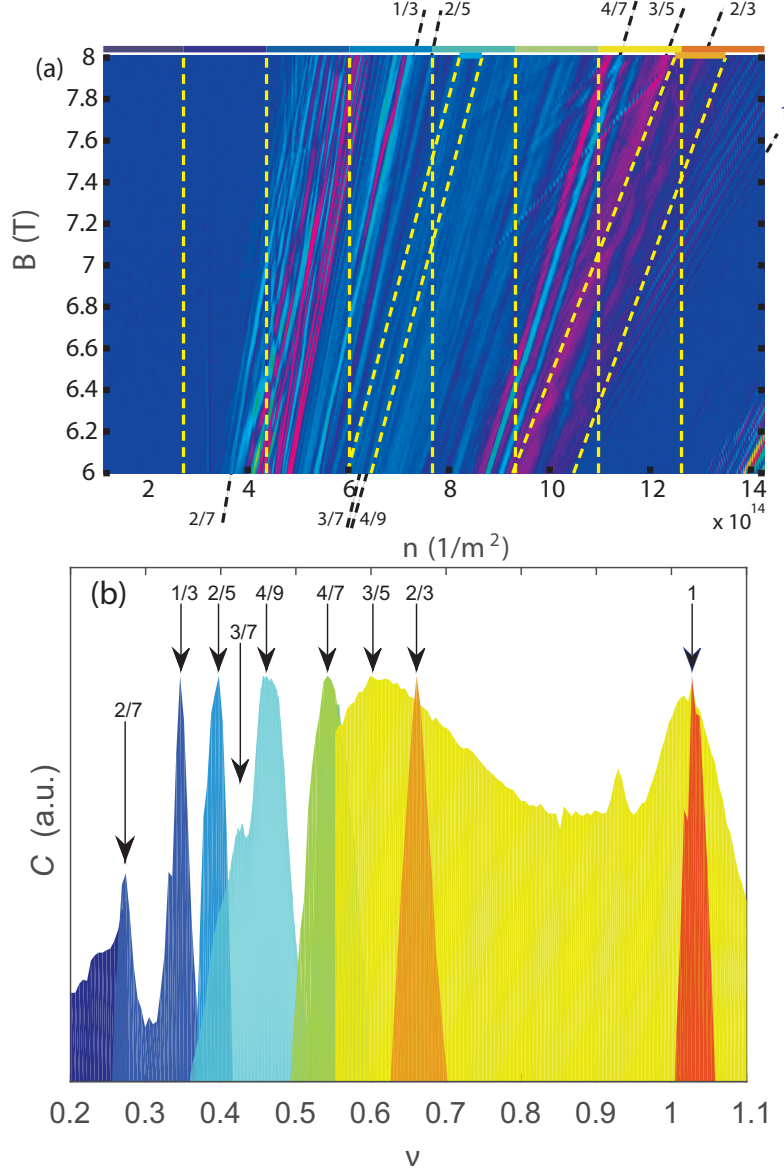


FIG. 3. (a) Modulation of transconductance phase $\text{Arg}\{g_m\}$ measured for sample EV over charge density n (V_g up to 15 V) at magnetic fields between 6 and 8 T (filling factor $\nu = 1$ is reached at the lowest right corner). The data are divided into ten regions, each marked with a color bar at the top of the stripe: we use eight vertical stripes of equal size and two inclined stripes which are defined in order to improve the contrast of fringes at $\nu = 3/7$ and $\nu = 2/3$. The correlation analysis has been performed separately in each region. The black dashed lines off the borders indicate FQH states with the marked fractional filling factor. (b) Scaled correlation $c(\nu) = h(\nu)/h(\nu)_{\max}$ as a function of the filling factor ν ; see text and the supplemental information for the definition of the correlation function $h(\nu)$. The color of the distribution refers to the color code of the analyzed regions in Fig. 3a. The peak values are marked with the corresponding fractional filling factors. The distinct FQH states are $\nu = \{2/7, 1/3, 2/5, 3/7, 4/9, 4/7, 3/5, 2/3\}$.

located at the boundary regions near the metallic contacts. Due to absence of any polarizing medium close to suspended graphene, the screening of charge near metallic contacts is rather weak. Consequently, strong doping from a metallic contact can extend appreciably in to the suspended graphene near the contact [30]. The amount of edge doping depends on the details of the metallic contacts, which may be in the range of $E_F \sim -100$ meV [31]. Such a doping corresponds to a charge density of $n_c = 7.2 \times 10^{11} \text{ 1/cm}^2 > eB/h$ under the contact metal, which is sufficient for accommodating QH states with $\nu = 2$.

III. WIGNER CRYSTALLIZATION

Non-linear electrical conductance provides a means to distinguish between several possible transport mechanisms, including activation of fractionally charged quasiparticles [27, 28] and depinning of Wigner crystal [32–36]. Our conductance at high T agrees with the thermal activation process [27, 28] and, in this regime, the data can be employed to determine estimates of the excitation energy gaps of the FQH states. At low temperatures, the conductance and IV characteristics display a more complex dependence on charge density. Our IV characteristics at low filling factor ($\nu = 0.16 \dots 0.33$) are illustrated in Fig. 4a for sample EV. At $\nu = 0.33$, the IV curve displays first a linear part that extends nearly up to $0.5 - 0.7$ mV, above which there is a strong increase in current in a power-law-like fashion as V^α . Such an IV curve can be understood by transport via quantum tunneling along a percolating path of several localized states where the non-linear regime would be a sign of competing higher order co-tunneling processes [37] within the path.

At filling factor $\nu = 0.20$, even the low voltage part appears as non-linear and it is difficult to resolve any Ohmic part in the IV curve, while at $\nu = 0.16$ there is a linear regime that is smaller than at $\nu = 0.33$. The behavior of our non-linear IV characteristics for sample XD is illustrated in Fig. 4b on semilog scale. The data at $\nu = 0.16$ display exponential increase in current between $V = 0.2 - 1.7$ mV. Exponential increase in current has been identified as gradual depinning of ordered charge carrier phase, having either Wigner solid or charge density wave (CDW) type of order [38]. According to theoretical calculations, Wigner crystal order is more likely than CDW at low charge density in graphene [39, 40]. Deviation of exponential behavior starts at $V_T = 1.7$ mV which is identified as the depinning threshold of Wigner crystal sliding. When $V < V_T$, charge transport takes place by thermally

activated hopping of pinned regions. Similar behavior was observed in sample EV, where we obtained a threshold voltage of $V_T = 1.2$ mV.

Following Ref. 35, we write for the current due to thermally activated motion of pinned crystallites below V_T as $I_W = e^* f_p \{\exp[-\frac{\bar{\Delta}-V/2N}{k_B T}] - \exp[-\frac{\bar{\Delta}+V/2N}{k_B T}]\}$, where f_p is the attempt frequency in the thermal escape process, $\bar{\Delta}$ is the average value of the pinning potential, and N denotes the number of Wigner crystallites in series across the transport path. In Fig. 4b, we obtain a good agreement between this basic theory and our experimental data at $\nu = 0.16$ using parameters $e^* = e$, $f_p = k_B T/h$, $\bar{\Delta} = 180$ μ eV, $N = 6$, and $T = 0.27$ K which is an estimate for average electronic temperature at 0.5 - 1 mV due to Joule heating. Note that $N\bar{\Delta}/e \simeq 1.1$ mV is close to the observed threshold voltage V_T . In Fig. 4b, we also depict measurement results at $\nu = 0.33$, the data of which have been fitted using a linear function. In agreement with Fig. 4a, the linear fit here extends quite well up to 0.5 mV.

The obtained average pinning potential $\bar{\Delta} = 180$ μ eV is quite large compared with observations in 2D electron gas devices in heterostructures [36]. One factor enhancing the observability of the Wigner crystal in suspended graphene may be provided by the deformation of the graphene sheet into a dimple lattice under the action of the back gate voltage. This would add inertia to the charge carriers as in the case of electrons on superfluid helium where the Wigner crystal has been observed even in the absence of magnetic field [41]. Such possibility of combining mechanical and electrical degrees of freedom for Wigner crystallization deserves further study in the future.

Fig. 4c displays the logarithm of total conductance $G_{tot} = I/V$ on the $\nu - V$ plane. The linear low-bias behavior of the IV curves at $\nu > 0.2$ is seen as constant conductance regions below the power-law regime. Above the power-law regime, G_{tot} gradually approaches the high-bias slope $dI/dV \sim 100$ k Ω . Fig. 4c indicates that conductance is strongly suppressed between $\nu = 0.12 - 0.20$, but good conductance re-emerges again at $\nu = 0.10 - 0.12$. We argue that, the presence of strongly insulating state at $\nu = 0.12 - 0.20$ in between FQH states is well in line with the presence of Wigner crystallization. In suspended graphene, Wigner crystallization may appear more distinctly than in other systems because the Coulomb energy is maximized due to the small electric permittivity of the vacuum environment. According to theory, the energy gaps in the FQH regime become smaller with decreasing filling fraction when $\nu < 1/3$. In our data, this tendency is not followed in the re-entrant regime, which lends additional support for the cross-over to Wigner crystal phase with

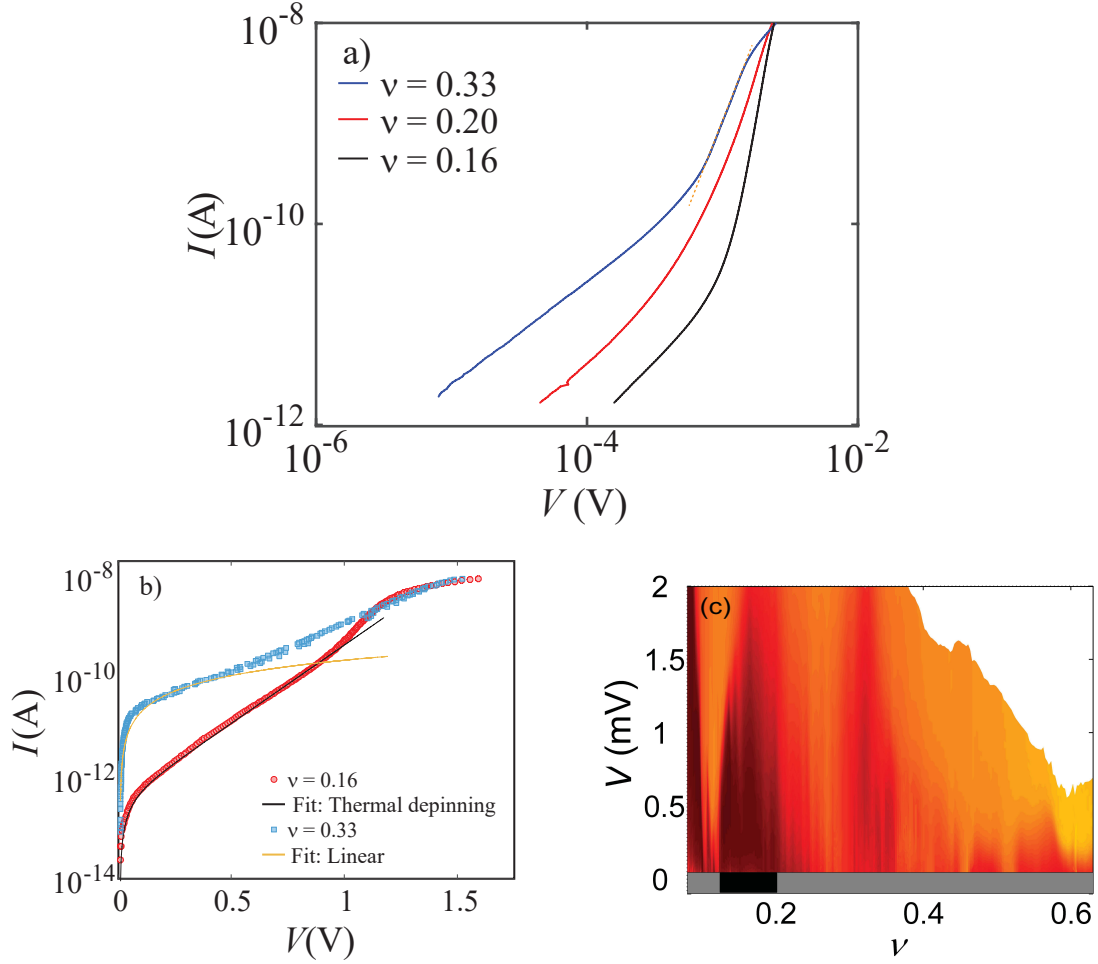


FIG. 4. (a) IV curves on log-log scale measured for sample EV at $B = 9$ T for fillings factors $\nu = 0.33$ (blue), 0.20 (red), and 0.16 (black). At low bias, the current at $\nu = 0.33$ displays linear behavior which indicates conduction via quantum tunneling along a percolating network of localized states. The fitted dashed line to $\nu = 0.33$ data in the non-linear regime indicates a power law with an exponent of $\alpha \sim 3.4$, most likely due to presence of cotunneling. (b) Semilog plot of two IV curves from sample XD corresponding to filling factors in frame (a): (\circ) $\nu = 0.16$ and (\square) $\nu = 0.33$. The black curve denotes a fit of I_W (see text) illustrating hopping transport in the Wigner crystal regime by thermally activated depinning of crystallites, while the orange curve displays linear IV behavior with a total resistance of $8 \text{ M}\Omega$ due to quantum tunneling over a chain of localized states. (c) Logarithm of conductance $G_{tot} = I/V$ measured as a function of bias voltage $V = 0 \dots 2$ mV over filling factors $\nu = 0.05 - 0.65$ at $B = 9$ T; orange color indicates high conductance and dark red shows reduced conductance (range spans $2 \cdot 10^{-5} - 1 \cdot 10^{-8}$ S). The Wigner crystal regime $\nu = 0.12 - 0.20$ is indicated by the black bar on the grey bottom stripe.

suppressed conductance.

IV. CONCLUSIONS

In conclusion, we have investigated fractional quantum Hall ordering in two-terminal suspended graphene Corbino devices where no edge states carry current across the sample. For bulk transport in the Corbino geometry, our measurements present a FQH sequence of $\{2/7, 1/3, 2/5, 3/7, 4/9, 4/7, 3/5, 2/3, 4/5, 9/7, 4/3\}$, which is an unparalleled sequence in transport measurements on two-lead graphene. At high T , our linear conductance is consistent with the thermal activation model developed in Refs. 27 and 28, but at low T , transport across our Corbino disk is much stronger than achievable by thermal activation, which we assign to quantum tunneling between broadened localized FQH levels. At low filling factors we observe competition between liquid and solid ordering, and our results support Wigner crystallization of electrons at $\nu = 0.20 - 0.12$ before the system re-enters FQH order around $\nu \simeq 0.1$, and finally switches to a gapped state near $\nu = 0$.

V. ACKNOWLEDGEMENTS

We thank C. Flindt, A. Harju, Y. Meir, T. Ojanen, S. Paraoanu, and E. Sonin for fruitful discussions. This work has been supported in part by the EU Framework Programme (FP7 and H2020 Graphene Flagship) and by the Academy of Finland (projects no. 250280 LTQ CoE and 286098).

VI. METHODS

A. Sample fabrication

Our sample fabrication is based on well-chosen combination of resists with differential selectivity, which allowed the fabrication steps for deposition of a suspended top contact (see supplemental material for details [23]). We exfoliated graphene (Graphenium form NGS Naturgraphit GmbH) using a heat-assisted exfoliation technique to maximize the size of the exfoliated flakes [42]. Monolayer graphene flakes were located by their contrast in an optical microscope and verified using a Raman spectrometer with He-Ne laser (633 nm).

The first contact defining the outer rim of the Corbino disk (see Fig. 1a) was deposited in the usual manner [43], and later the inner contact was fabricated along with an air bridge to connect the inner contact to a bonding pad. Strongly doped silicon Si++ substrate with 285 nm of thermally grown SiO₂ was used as a global back gate.

Due to the exposure of graphene to resists during the fabrication process, our suspended devices tend to be highly doped (mostly p-type) in our first resistance R vs. gate voltage V_g scans. Annealing of samples on LOR was typically performed at a bias voltage of 1.6 ± 0.1 V which is quite comparable with our HF etched, rectangular two-lead samples [44]. For further details on annealing, we refer to the supplemental information [23].

B. Measurement techniques

Our measurements down to 20 mK were performed in a BlueFors LD-400 dilution refrigerator. The measurement lines were twisted pair phosphor-bronze wires supplemented by three stage RC filters with a nominal cut-off given by $R = 100$ Ohms and $C = 5$ nF. However, due high impedance of the quantum Hall samples the actual cutoff is determined by the sample resistance. For magneto-conductance measurement, we used an AC peak-to-peak current excitation of 0.1 nA at $f = 3.333$ Hz.

Theoretical dependence of G vs V_g for a graphene Corbino sample at $B = 0$ was fitted to measured data in order to deduce an estimate for the contact resistance [23]. This fitting yielded for the typical value of the contact resistance $R_C \simeq 400 \Omega$. In our understanding, the estimated R_C is mostly related to the inner contact with a perimeter of 2.5 microns, which yields a 1-k Ω contact resistance per micron in accordance with our other graphene samples [45]. For details on the R_C determination, we refer to the supplemental information [23].

For transconductance $g_m = dI/dV_g$ we measured both magnitude $\text{Mag}\{g_m\}$ and phase $\text{Arg}\{g_m\}$ using low frequency lock-in detection. The best results for g_m correlation analysis were obtained by recording $\text{Arg}\{g_m\}$ at a bias voltage V that corresponded to the onset of the V^α regime, see Fig. 4a. Consistent information was obtained by analyzing the simultaneously obtained $\text{Mag}\{g_m\}$. The gate frequency in AC transconductance measurements was set at $f = 17.777$ Hz, while the peak-to-peak AC excitation amplitude was adjusted to correspond to charge of one electron over the sample. The DC bias between source and

drain was varied in the range $V = 0.1 - 0.5$ mV.

In addition to the field effect mobility, we characterized our samples in terms of quantum mobility [46]. Shubnikov - de Haas oscillations were well visible in the range $B = 0.1 - 0.5$ T, which is in agreement with quantum mobility of $\mu_q \sim 6 \times 10^4$ cm²/Vs deduced from the decay of the amplitude of the SdH oscillations (see the supplemental information). The quantum scattering time $\simeq 0.3$ ps calculated from the decay of SdH oscillations indicates that the width of Landau levels is in order of ~ 10 Kelvin.

The location of the Dirac point and the gate capacitance were fixed by the Landau fan obtained in conductance scans $G(B, n)$. At $B = 9$ T, the residual charge density and spread in Dirac point location amount to an uncertainty up to 0.05 in the filling factor ν .

-
- [1] D. C. Tsui, H. L. Stormer, and A. C. Gossard, “Two-dimensional magnetotransport in the extreme quantum limit,” *Phys. Rev. Lett.* **48**, 1559–1562 (1982).
 - [2] Kirill I. Bolotin, Fereshte Ghahari, Michael D. Shulman, Horst L. Stormer, and Philip Kim, “Observation of the fractional quantum Hall effect in graphene,” *Nature* **462**, 196–199 (2009).
 - [3] Xu Du, Ivan Skachko, Fabian Duerr, Adina Luican, and Eva Y. Andrei, “Fractional quantum Hall effect and insulating phase of Dirac electrons in graphene,” *Nature* **462**, 192–195 (2009).
 - [4] Fereshte Ghahari, Yue Zhao, Paul Cadden-Zimansky, Kirill Bolotin, and Philip Kim, “Measurement of the $\nu=1/3$ fractional quantum Hall energy gap in suspended graphene,” *Phys. Rev. Lett.* **106**, 046801 (2011).
 - [5] D. A. Abanin, I. Skachko, X. Du, E. Y. Andrei, and L. S. Levitov, “Fractional quantum Hall effect in suspended graphene: Transport coefficients and electron interaction strength,” *Phys. Rev. B* **81**, 115410 (2010).
 - [6] I. Skachko, X. Du, F. Duerr, A. Luican, D. A. Abanin, L. S. Levitov, and E. Y. Andrei, “Fractional quantum Hall effect in suspended graphene probed with two-terminal measurements,” *Philos. Trans. A. Math. Phys. Eng. Sci.* **368**, 5403–5416 (2010).
 - [7] C. R. Dean, A. F. Young, P. Cadden-Zimansky, L. Wang, H. Ren, K. Watanabe, T. Taniguchi, P. Kim, J. Hone, and K. L. Shepard, “Multicomponent fractional quantum Hall effect in graphene,” *Nat. Phys.* **7**, 693–696 (2011).
 - [8] X. Lin, R. R. Du, and X. C. Xie, “Recent experimental progress of fractional quantum Hall

- effect: $5/2$ filling state and graphene,” Natl. Sci. Rev. **1**, 564–579 (2014).
- [9] Benjamin E Feldman, Benjamin Krauss, J. H. Smet, and Amir Yacoby, “Unconventional sequence of fractional quantum Hall states in suspended graphene,” Science **337**, 1196–1199 (2012).
 - [10] Benjamin E. Feldman, Andrei J. Levin, Benjamin Krauss, Dmitry A. Abanin, Bertrand I. Halperin, Jurgen H. Smet, and Amir Yacoby, “Fractional quantum Hall phase transitions and four-flux states in graphene,” Phys. Rev. Lett. **111**, 076802–5 (2013).
 - [11] Dong Su Lee, Viera Skakalova, R. Thomas Weitz, Klaus Von Klitzing, and Jurgen H. Smet, “Transconductance fluctuations as a probe for interaction-induced quantum Hall states in graphene,” Phys. Rev. Lett. **109**, 056602 (2012).
 - [12] Landau Level mixing scales with Coulomb interaction energy; the fractional states of electron survives such a strong Landau Level mixing [47].
 - [13] Changyao Chen, Vikram V Deshpande, Mikito Koshino, Sunwoo Lee, Alexander Gondarenko, Allan H. MacDonald, Philip Kim, and James Hone, “Modulation of mechanical resonance by chemical potential oscillation in graphene,” Nat. Phys. **12**, 240–244 (2015).
 - [14] E. Wigner, “On the interaction of electrons in metals,” Phys. Rev. **46**, 1002–1011 (1934).
 - [15] J. Sólyom, “Wigner crystals: New realizations of an old idea,” EPJ Web Conf. **78**, 01009 (2014).
 - [16] R. B. Laughlin, “Quantized Hall conductivity in two dimensions,” Phys. Rev. B **23**, 5632–5633 (1981).
 - [17] V. T. Dolgoplov, N. B. Zhitenev, and A. A. Shashkin, “New method for determining Hall conductivity in QHE regime,” Europhys. Lett. **14**, 255–259 (1991).
 - [18] V. T. Dolgoplov, A. A. Shashkin, N. B. Zhitenev, S. I. Dorozhkin, and K. Von Klitzing, “Quantum Hall effect in the absence of edge currents,” Phys. Rev. B **46**, 12560–12567 (1992).
 - [19] F. Hohls, U. Zeitler, and R. J. Haug, “High frequency conductivity in the quantum Hall regime,” Phys. Rev. Lett. **86**, 5124–5127 (2001).
 - [20] B. A. Schmidt, K. Bennaceur, S. Bilodeau, G. Gervais, L. N. Pfeiffer, and K. W. West, “Second Landau level fractional quantum Hall effects in the Corbino geometry,” Solid State Commun. **217**, 1–5 (2015).
 - [21] Yue Zhao, Paul Cadden-Zimansky, Fereshte Ghahari, and Philip Kim, “Magnetoresistance measurements of graphene at the charge neutrality point,” Phys. Rev. Lett. **108**, 106804 (2012).

- [22] Eva C. Peters, A. J. M. Giesbers, Marko Burghard, and Klaus Kern, “Scaling in the quantum Hall regime of graphene Corbino devices,” *Appl. Phys. Lett.* **104**, 203109 (2014), 10.1063/1.4878396.
- [23] Manohar Kumar, Antti Laitinen, and Pertti J. Hakonen, “Supplemental information for fractional quantum Hall effect and Wigner crystallization in suspended Corbino graphene disk,” .
- [24] Adam Rycerz, Patrik Recher, and Michael Wimmer, “Conformal mapping and shot noise in graphene,” *Phys. Rev. B* **80**, 125417 (2009).
- [25] S Ilani, J Martin, E Teitelbaum, J H Smet, D Mahalu, V Umansky, and A Yacoby, “The microscopic nature of localization in the quantum Hall effect,” *Nature* **427**, 328–332 (2004).
- [26] Jens Martin, Shahal Ilani, Basile Verdene, Jurgen Smet, Vladimir Umansky, Diana Mahalu, Dieter Schuh, Gerhard Abstreiter, and Amir Yacoby, “Localization of fractionally charged quasi-particles,” *Science* **305**, 980–983 (2004).
- [27] D. G. Polyakov and B. I. Shklovskii, “Universal prefactor of activated conductivity in the quantum Hall effect,” *Phys. Rev. Lett.* **74**, 150–153 (1995).
- [28] N. D’Ambrumenil, B. I. Halperin, and R. H. Morf, “Model for dissipative conductance in fractional quantum Hall states,” *Phys. Rev. Lett.* **106**, 126804 (2011).
- [29] Masayuki Hashisaka, Tomoaki Ota, Koji Muraki, and Toshimasa Fujisawa, “Shot-noise evidence of fractional quasiparticle creation in a local fractional quantum hall state,” *Phys. Rev. Lett.* **114**, 056802 (2015).
- [30] P. A. Khomyakov, A. A. Starikov, G. Brocks, and P. J. Kelly, “Nonlinear screening of charges induced in graphene by metal contacts,” *Phys. Rev. B* **82**, 115437 (2010).
- [31] Antti Laitinen, G. S. Paraoanu, Mika Oksanen, Monica F. Craciun, Saverio Russo, Edouard Sonin, and Pertti Hakonen, “Contact doping, Klein tunneling, and asymmetry of shot noise in suspended graphene,” *Phys. Rev. B* **93**, 115413 (2016).
- [32] R. L. Willett, H. L. Stormer, D. C. Tsui, L. N. Pfeiffer, K. W. West, and K. W. Baldwin, “Termination of the series of fractional quantum Hall states at small filling factors,” *Phys. Rev. B* **38**, 7881–7884 (1988).
- [33] H. W. Jiang, R. L. Willett, H. L. Stormer, D. C. Tsui, L. N. Pfeiffer, and K. W. West, “Quantum liquid versus electron solid around $\nu=1/5$ Landau-level filling,” *Phys. Rev. Lett.* **65**, 633–636 (1990).

- [34] V. J. Goldman, M. Santos, M. Shayegan, and J. E. Cunningham, “Evidence for two-dimensional quantum Wigner crystal,” *Phys. Rev. Lett.* **65**, 2189–2192 (1990).
- [35] F. I. B. Williams, P. A. Wright, R. G. Clark, E. Y. Andrei, G. Deville, D. C. Glattli, O. Probst, B. Etienne, C. Dorin, C. T. Foxon, and J. J. Harris, “Conduction threshold and pinning frequency of magnetically induced Wigner solid,” *Phys. Rev. Lett.* **66**, 3285–3288 (1991).
- [36] M. Shayegan, “Perspectives in quantum Hall effects: novel quantum liquids in low-dimensional semiconductor structures,” (eds. Sarma, Das S. and Pinczuk, A., Wiley, 1997) Chap. Case for the Magnetic-Field-Induced Two-Dimensional Wigner Crystal, p. 343.
- [37] D. V. Averin and Yu V. Nazarov, “Virtual electron diffusion during quantum tunneling of the electric charge,” *Phys. Rev. Lett.* **65**, 2446–2449 (1990).
- [38] G. Grüner, “The dynamics of charge-density waves,” *Rev. Mod. Phys.* **60**, 1129–1181 (1988).
- [39] C.-H. Zhang and Yogesh N. Joglekar, “Wigner crystal and bubble phases in graphene in the quantum Hall regime,” *Phys. Rev. B* **75**, 245414 (2007).
- [40] Hao Wang, D. N. Sheng, L. Sheng, and F. D M Haldane, “Broken-symmetry states of Dirac fermions in graphene with a partially filled high Landau level,” *Phys. Rev. Lett.* **100**, 116802 (2008).
- [41] Keiya Shirahama and Kimitoshi Kono, “Dynamical transition in the Wigner solid on a liquid helium surface,” *Phys. Rev. Lett.* **74**, 781–784 (1995).
- [42] Yuan Huang, Eli Sutter, Norman N. Shi, Jiabao Zheng, Tianzhong Yang, Dirk Englund, Hong Jun Gao, and Peter Sutter, “Reliable exfoliation of large-area high-quality flakes of graphene and other two-dimensional materials,” *ACS Nano* **9**, 10612–10620 (2015).
- [43] Nikolaos Tombros, Alina Veligura, Juliane Junesch, J. Jasper van den Berg, Paul J. Zomer, Magdalena Wojtaszek, Ivan J. Vera Marun, Harry T. Jonkman, and Bart J. van Wees, “Large yield production of high mobility freely suspended graphene electronic devices on a polydimethylglutarimide based organic polymer,” *J. Appl. Phys.* **109**, 093702 (2011).
- [44] Antti Laitinen, Mika Oksanen, Aurélien Fay, Daniel Cox, Matti Tomi, Pauli Virtanen, and Pertti J. Hakonen, “Electron-phonon coupling in suspended graphene: Supercollisions by ripples,” *Nano Lett.* **14**, 3009–3013 (2014).
- [45] S. Russo, M.F. Craciun, M. Yamamoto, A.F. Morpurgo, and S. Tarucha, “Contact resistance in graphene-based devices,” *Physica E: Low-dimensional Systems and Nanostructures* **42**, 677 – 679 (2010).

- [46] Tsuneya Ando, Alan B. Fowler, and Frank Stern, “Electronic properties of two-dimensional systems,” *Rev. Mod. Phys.* **54**, 437–672 (1982).
- [47] Michael R. Peterson and Chetan Nayak, “Effects of Landau level mixing on the fractional quantum Hall effect in monolayer graphene,” *Phys. Rev. Lett.* **113**, 086401 (2014).

Supplementary Information: Fractional quantum Hall effect and Wigner crystallization in suspended Corbino graphene disk

Manohar Kumar, Antti Laitinen and Pertti J. Hakonen

In this supplement we provide additional information on sample fabrication, current annealing of graphene to enhance mobility, residual charge doping near the Dirac point, determination of mobility and contact resistance, results on Shubnikov de Haas oscillations, and the identification of fractional states using transconductance.

VII. SAMPLE FABRICATION

Our sample fabrication is based on well-chosen combination of resists with differential selectivity, which allowed the fabrication steps for the deposition of a suspended top contact. In this work, we employed heat assisted mechanical exfoliation technique [42]. The application of heat assisted exfoliation on top of LOR resist produced large graphene flakes, which was the basic requirement for a good Corbino device. A 250 + 250 nm thick base layer of LOR-3A [43] was spun in two steps on SiO₂/Si++ and baked at 200°C for 5 and 12 min, respectively. A graphite covered tape was pressed against the LOR-covered wafer for 1 min and subsequently baked on a hot plate at 100°C for 2 min. The tape was peeled from the chip after it had cooled down to room temperature. The exfoliated graphene flake was first characterized optically and then using Raman spectroscopy at 633 nm.

In the first lithography step, the lead for the outer ring and its contact pad were fabricated. A double layer PMMA (950K/A3: top layer and 50K/A11: bottom layer) spun and patterned using e-beam. A Cr/Au sandwich of 5/70 nm thickness was evaporated at pressure $p < 6 \times 10^{-8}$ mBar. After metal deposition, special care was taken during the metal lift-off process: the lift off was performed in 80°C xylene and the unwanted residual metal from the circular hole of outer lead was removed using micromanipulation. The outer ring electrode is of rectangular geometry extending over the graphene flake with a circular hole of diameter 2 – 10 μm , see Fig.5c. On the processed sample, another 500 nm thick LOR was spun. A via in the center of the circular hole of outer lead was opened in the top

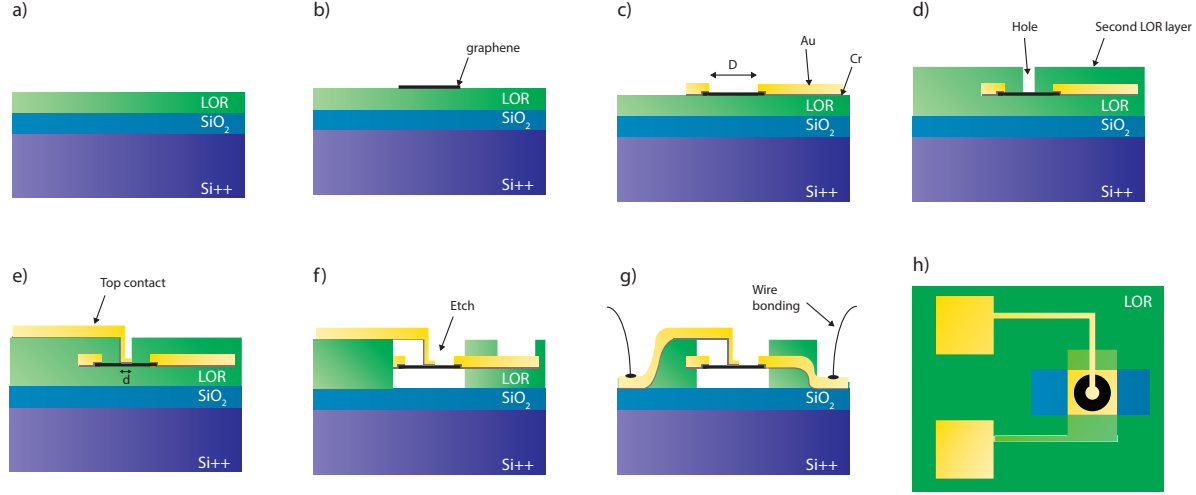


FIG. 5. Fabrication process steps: a) LOR layer with thickness of ~ 500 nm is spun on a cleaned Si/SiO₂ chip. b) Mechanical exfoliation of graphene on top of the LOR layer. c) Fabrication of outer lead and its bonding pad. d) Formation of a via for the inner lead using a second LOR layer. e) Air bridge connecting inner lead and pad is patterned using an e-beam lithography step with PMMA. f) Suspension of graphene between the inner and outer leads and uncovering of the outer lead-pad by e-beam exposure. g) Status after wire bonding: gold pads are deformed and pushed partly down to silicon. h) A schematic top view of a sample with suspended top contact: black color shows suspended graphene, blue color shows the exposed window in LOR, light yellow color shows the covered outer lead and bright yellow color indicates clean gold of the inner lead and the outer leads.

LOR layer using e-beam lithography. A dose of $1000 \mu\text{C}/\text{cm}^2$ was used for this step. The exposed pattern was developed in ethyl lactate for 60 s and rinsed in hexane. The diameter of the via varied between $0.5 - 5 \mu\text{m}$, see Fig.5d. This via acts as foundation for the inner electrode contact in the concentric Corbino geometry. For fabrication of the inner lead, a double layer PMMA of 200 nm was spun and patterned using e-beam lithography. On the patterned device, Cr (5 nm)/Au (100 nm) was deposited, and the subsequent lift off was done in hot xylene with a rinse in hexane, see Fig. 5e.

In final steps of the lithography, the graphene between inner and outer ring leads was suspended by exposing LOR to a dose of $1000 \mu\text{C}/\text{cm}^2$. In order to expose the outer lead bonding pad, LOR on the larger structures was exposed to an e-beam dose of $700 \mu\text{C}/\text{cm}^2$.

The device was developed and cleaned in ethyl lactate for 60s and rinsed in hexane for 60s. A schematic cross section of the final device is depicted in Fig. 5f and an SEM image of a complete sample structure is shown in Fig. 1a of main text. For bonding, part of the pad was pressed against the SiO₂, as shown in Fig. 5g. These pressed pads were used for bonding. The finished devices were electrically characterized at room temperature, and devices with low resistance were selected for low temperature measurements.

VIII. ANNEALING

After fabrication, our suspended Corbino graphene samples were predominantly of *p*-type. During typical annealing process, the doping shifts to *n*-type before reaching the desired charge-neutral state. For achieving charge neutrality, a high current annealing was performed. We employed voltage bias for our current annealing process: In contrast to current-biased devices, voltage-biased samples are protected against spurious rise in resistance due to shifting of the Dirac point. A typical bias voltage value used in annealing of our samples was 1.6 ± 0.1 V; in spite of strong heating of the refrigerator, the sample was kept at temperatures $T < 1$ K during annealing. Slight asymmetry in the concentricity of the electrodes in our Corbino geometry, inverse radial decay of current, and local variation of the contact resistance result in non-uniformity of current annealing. Owing to this non-uniformity, our suspended Corbino disk becomes split into differently annealed graphene domains, each having their own charge neutrality point. This can be seen in Fig. 6. Eventually, during annealing process several of these peaks merge to give a single Dirac peak or closely degenerate Dirac peaks.

IX. RESIDUAL DOPING

The level of residual charge doping was extracted from G vs n -plots on *loglog*-scale as the point where conductance G levels off when approaching the Dirac point. We employed straight line fits (power laws with exponent around 1/2) to the conductance data in order to better define the position of this cross-over point, as shown in Fig. 7.

The residual doping for other samples was extracted in the same way: $n_{0,\text{XD}} = 2 \times 10^{10}$ 1/cm² and $n_{0,\text{EV}} = 6 \times 10^9$ 1/cm². The residual density modulation n_0 amounts to about

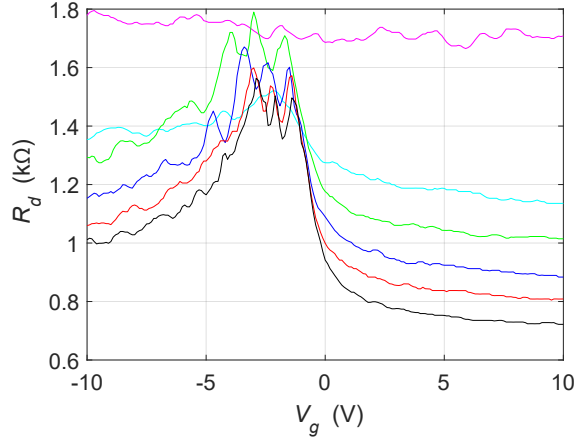


FIG. 6. Annealing progress of a Corbino sample with outer diameter $D = 3.2 \mu\text{m}$ and inner contact diameter $d = 0.8 \mu\text{m}$. The magenta curve at the top is the first differential resistance R_d trace measured after annealing current $I \approx 1.5 \text{ mA}$ ($V \approx 1.3 \text{ V}$) while the black curve, obtained after $I \approx 2 \text{ mA}$ ($V \approx 1.7 \text{ V}$), denotes the final annealing result (sample EV in Table I of the main paper).

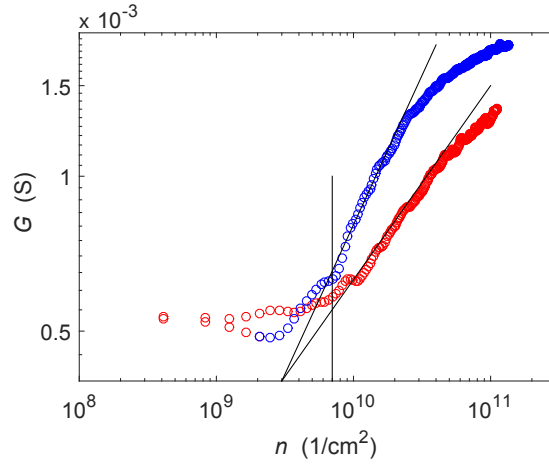


FIG. 7. G vs n for sample EV* on *loglog*-scale: red and blue circles represent data on the hole and electron sides, respectively. The black lines represent power law trends in the data. The corner point of the curves (coinciding with the intersection of the lines with different doping) is taken as n_0 , which yields here $n_0 = 6 \times 10^9 \text{ 1/cm}^2$. No contact resistance was subtracted in this analysis.

15 and 30% of the Wigner crystal charge density $n = 2.6 - 4.4 \cdot 10^{10} \text{ 1/cm}^2$ in samples EV and XD, respectively.

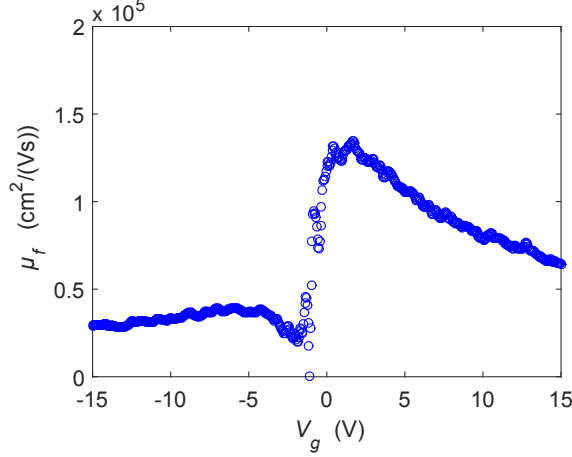


FIG. 8. Sample EV*: calculated mobility as a function of gate voltage. Contact resistance of $R_c = 410 \, \Omega$ has been subtracted off from the resistance, *i.e.*, $G = \frac{1}{R-R_c}$ in this analysis.

X. MOBILITY

Field effect mobility of our samples (see Fig. 8 for data on sample EV*) was calculated using the formula

$$\mu_f = \frac{\sigma - \sigma_0}{ne}, \quad (1)$$

where σ_0 is the measured minimum conductivity, and n denotes the charge carrier density. The conductivity in Corbino geometry can be calculated from measured conductance G using

$$\sigma = G \frac{\ln(r_o/r_i)}{2\pi}, \quad (2)$$

where r_o and r_i are the radii of outer and inner contacts, respectively.

When calculating the mobility using Eqs. 1 and 2, we take into account the contact resistance R_c . We estimate R_c from the comparison of measured data to the theory based on evanescent mode transport [24]. Fig. 9 displays such a fitting for sample EV*, which yields $R_c = 410 \, \Omega$ for the contact resistance. After this procedure, we obtain μ_f reaching up to $1.4 \times 10^5 \, \text{cm}^2/\text{Vs}$, as seen in Fig. 8.

For our other samples the following mobilities were extracted with the same procedure: $\mu_{f,\text{XD}} \approx 4 \times 10^4 \, \text{cm}^2/\text{Vs}$ and $\mu_{f,\text{EV}} \approx 2.0 \times 10^5 \, \text{cm}^2/\text{Vs}$. These values are listed in Table I in the main paper.

XI. EXTRACTING CONTACT RESISTANCE

Transport properties of a graphene Corbino disk were calculated in Ref. 24. The conductance is determined by

$$G = \frac{se^2}{h} \sum_{j=\frac{1}{2}, \frac{3}{2}, \frac{5}{2}, \dots} T_j, \quad (3)$$

where $s = 8$ and T_j is the transmission coefficient of the j th channel. Transmission coefficient is given by

$$T_j = \frac{16}{\pi^2 k^2 R_1 R_2} \frac{1}{(\mathfrak{D}_j^+)^2 + (\mathfrak{D}_j^-)^2}, \quad (4)$$

with

$$\begin{aligned} \mathfrak{D}_j^\pm = & \Im \{ H_{j-1/2}^{(1)}(kr_i) H_{j\mp 1/2}^{(2)}(kr_o) \\ & \pm H_{j+1/2}^{(1)}(kr_i) H_{j\pm 1/2}^{(2)}(kr_o) \}, \end{aligned} \quad (5)$$

where $H_\nu^{(K)}(x)$ is the K th Hankel function and $k = \sqrt{\pi|n|}$ denotes the wave vector.

By using Eq. 3 one can generate theoretical curves corresponding to our devices. In Fig. 9, the measured conductance is compared with the theoretical curve and they are found to agree well when a contact resistance of 410 Ω is taken into account. Note that if we would linearize the dependence of G vs. n using R_c , a procedure which is expected to be valid for long-range Coulomb scattering, then the contact resistance would grow from the above value. We conjecture that most of this contact resistance is at the inner contact electrode, leading to a contact resistance of 1 k Ω per micrometer, which is quite close to the experimental findings of Ref. 45.

XII. SHUBNIKOV DE HAAS OSCILLATIONS AND QUANTUM MOBILITY

Samples were characterized at low magnetic fields around a few hundred mT using Shubnikov-de Haas oscillations (the well-defined quantum Hall states in our samples first develop around 0.5 T). These oscillations yield information about the characteristic properties of charge carriers like mobility, quantum life time of carriers, and their effective mass. The diagonal resistance R_{xx} oscillates periodically with inverse magnetic field, while temperature suppresses these oscillation due to enhanced scattering of carriers. The variation

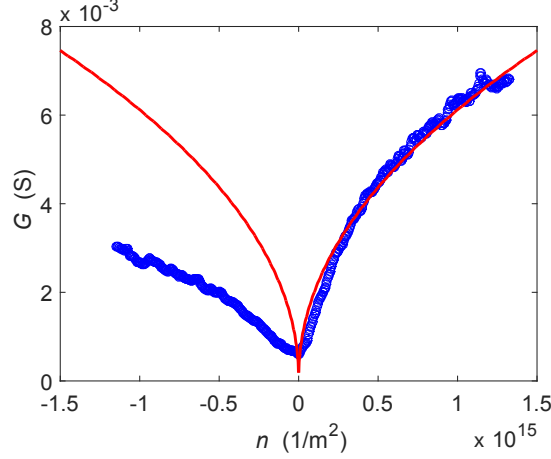


FIG. 9. DC conductance measured for sample EV* (blue circles). The solid red curve illustrates a theoretical fit which agrees with the data when the contact resistance is set to $R_c = 410 \, \Omega$, *i.e.*, $G = \frac{1}{R-R_c}$ for the data points.

of resistance is given by equation [46]:

$$\frac{R_{xx}}{R_0} = 1 + 4 \frac{X}{\sinh(X)} \exp\left(-\frac{\pi}{\mu_q B}\right) \cos\left(\pi \frac{E_F}{\hbar \omega_c} - \theta\right), \quad (6)$$

where R_0 is the resistance at zero field, $X(T) = 2\pi^2 k_B T / \hbar \omega_c$ with cyclotron frequency $\omega_c = eB/m^*$, E_F specifies the Fermi level, μ_q denotes the quantum mobility of charge carriers, and θ is a phase factor. Looking at resistance oscillations alone, Eq. 6 can be written as

$$\Delta R_{xx} = A \cdot \exp\left(-\frac{\pi}{\mu_q B}\right) \cdot \cos\left(\pi \cdot \frac{E_F}{\hbar \omega_c} - \theta\right), \quad (7)$$

with A as a constant defined by $X(T)$.

Fig. 10 displays the SdH oscillations seen in sample EV. The quantum mobility obtained from the fit amounts to $\mu_q \simeq 6 \times 10^4 \, \text{cm}^2/\text{Vs}$, which is by a factor of three smaller than the value of the field effect mobility in Table I of the main paper. This value for μ_q corresponds to the quantum scattering time $\tau_d \simeq 0.3 \, \text{ps}$ which yields for the Landau level width $\delta_{LL} = \hbar/2\tau_q \simeq 10 \, \text{K}$.

In order to achieve a better analysis of the oscillations themselves, a base line marked by the red line in Fig. 10 was subtracted from R . These pure oscillations are displayed in Fig. 11. Quantum mobility was extracted from the envelope curve of these oscillations, as indicated in Fig. 11. In the case of sample EV, the quantum mobility is $\mu_q = 6 \times 10^4 \, \text{cm}^2/\text{Vs}$ (red lines in Fig. 11).

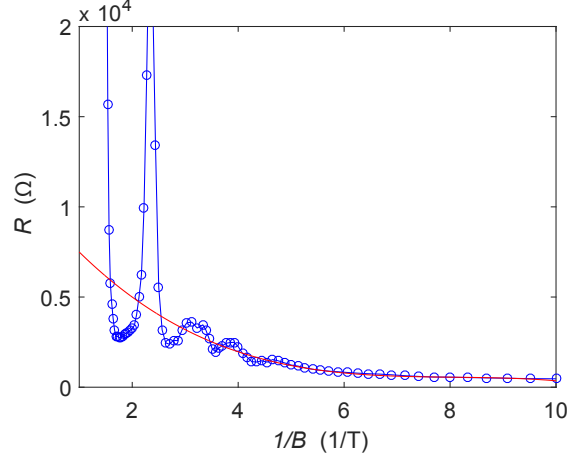


FIG. 10. (\circ) Resistance of sample EV as a function of the inverse of the perpendicular magnetic field $1/B$. Shubnikov de Haas oscillations are visible around the base line indicated by the red curve.

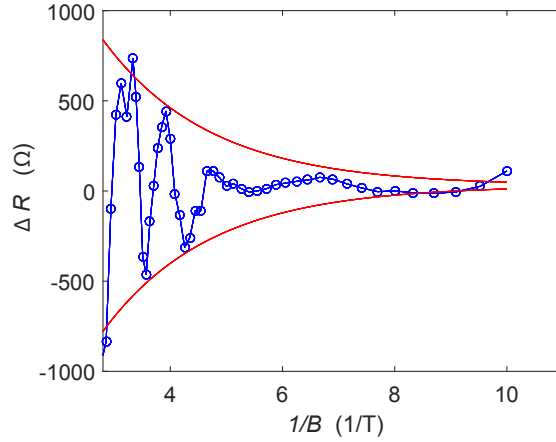


FIG. 11. Shubnikov de Haas oscillations around the subtracted base line (red curve in Fig. 10). The solid red curves represent envelope of the oscillations and they correspond to quantum mobility $\mu_q = 6 \times 10^4 \text{ cm}^2/\text{Vs}$.

XIII. IDENTIFICATION AND ANALYSIS OF TRANSCONDUCTANCE LINES

The transconductance g_m measurements were performed to identify the fragile fractional quantum Hall states in a well-controlled, indisputable manner. For $g_m(n, B)$ measurement, an ac excitation of the 2.7 mV_{rms} is applied to the back gate on top of the dc voltage, and sample is voltage biased with $V \sim 0.1 - 3 \text{ mV}$. Both X and Y components of the

current modulation were recorded using a lock-in amplifier. The gate modulation frequency was selected to correspond to the roll-off frequency of RC time constant, governed by the sample resistance of a few megaohms. Consequently, the change in g_m was observed both in the phase angle and amplitude of the recorded signal. It turned out that, when using long integration times in our lock-in detection, the phase signal was easier to analyze for identification of FQH states than the amplitude signal. Hence, we found our analysis mostly on the phase of the transconductance signal.

Transconductance-based Landau fan type of diagram for sample XD is displayed in Fig. 12. Compared with Fig. 2a in the main paper, this scan has more overlapping fringes, which tends to broaden the observed features and to smear the results of the correlation analysis. The number of visible features indicates a stronger disorder potential present in this device compared with sample EV, which is in agreement with the worse field-effect mobility listed in Table I for sample XD.

The FQH state signatures in g_m are identified using correlation analysis, which is based on the work of Lee *et al.* [11]. A line with a slope corresponding to a filling factor ν , is drawn on the pixel map of $g_m(n, B)$ and the nearest pixels (n_i, B_j) are selected. The values at selected points (n_i, B_j) are transferred to vectors A_k^w where the index k covers the full line and the index w keeps track of the vertical (B) coordinate of the drawn lines (see Fig. 13). The cross-correlation $h(\nu)^w$ of pixels within a single vector A_k^w is calculated using

$$h(\nu)^w = \frac{1}{S} \sum_{kl} A_k^w \cdot A_l^w (1 - \delta_{kl}), \quad (8)$$

where the Kronecker delta δ_{kl} removes the auto-correlation part from the function and S is total number of pixel products in summation over k and l . The total unscaled correlation function is obtained by summing over all values of w : $h(\nu) = \sum_w h(\nu)^w$. In order to find dominant fractional slopes in the data, the cross-correlation was calculated for all $\nu \in \{0...1.5\}$ and histograms of $h(\nu)$ were plotted. A peak in the correlation histogram indicates presence of dominating feature corresponding to the filling factor ν . For better inter-comparison of different analyzed regions, we scale our correlation histogram by the maximum correlation: $c(\nu) = h(\nu)/h(\nu)_{max}$.

The correlation map for sample XD is shown in Fig. 14. As already mentioned above, the correlation peaks in this picture are broadened in comparison with Fig. 2b of the main paper. This is because the disorder potential in sample XD is larger than in EV. Interestingly, this

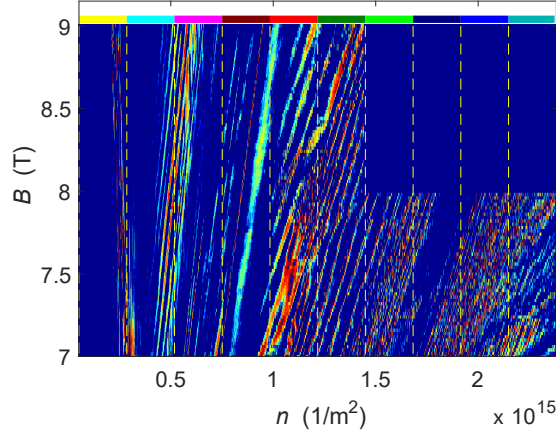


FIG. 12. The measured transconductance phase data at high field 7–9 T for sample XD (the blank upper right corner was not scanned in the experiment). The yellow lines mark the boundaries of the sections in which the correlation function was evaluated. The color on top of each stripe corresponds to the analyzed histogram in Fig. 14.

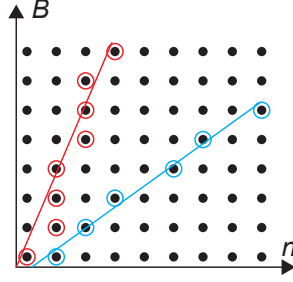


FIG. 13. Vector A_k^w with slope ν is formed by selecting a line $y = \nu x + w$ on the measured $n - B$ plane and taking the pixels closest to the line on each row (*i.e.* a particular field B) as illustrated in the figure. Blue and red lines correspond to filling factor slopes ν_1 and ν_2 , respectively, and the black dots denote data pixels: the selected data points for correlation analysis are indicated by blue and red circles for these two filling factors.

histogram picture gives evidence of the fractional state $4/5$ which was absent in sample EV, though it was present in the conductance Landau fan diagram of sample EV*. Hence, a proper amount (or shape) of disorder potential appears to enhance the visibility of FQH in bulk graphene transport measurements.

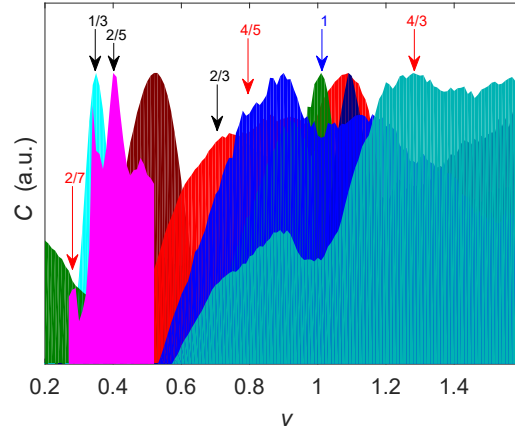


FIG. 14. Scaled correlation function $c(\nu)$ obtained from the data in Fig. 12. The identified fractional states are marked by arrows; states marked in red could not be resolved in our highest-mobility sample EV.